

**Silicon Carbide (SiC) Derived from Agricultural Waste  
Potentially Competitive with Silicon Anodes**

Journal:	<i>Green Chemistry</i>
Manuscript ID	GC-ART-02-2022-000645.R1
Article Type:	Paper
Date Submitted by the Author:	07-Apr-2022
Complete List of Authors:	Yu, Mengjie; University of Michigan, Temeche, Eleni; University of Michigan, Materials Science and Engineering Indris, Sylvio; Karlsruhe Institut fur Technologie, Institute for Applied Materials Lai, Wei; Michigan State University, Chemical Engineering and Materials Science Laine, Richard; University of Michigan, Materials Science and Eng.

# Silicon Carbide (SiC) Derived from Agricultural Waste Potentially Competitive with Silicon Anodes

*Mengjie Yu,<sup>1</sup> Eleni Temeche,<sup>2</sup> Sylvio Indris,<sup>3</sup> Wei Lai,<sup>4</sup> and Richard M. Laine\* <sup>1,2</sup>*

1. Macromolecular Science and Engineering, University of Michigan, Ann Arbor, Michigan 48109, USA
2. Department of Materials Science and Engineering, University of Michigan, Ann Arbor, Michigan 48109, USA
3. Institute for Applied Materials-Energy Storage Systems (IAM-ESS), Karlsruhe Institute of Technology (KIT), Eggenstein-Leopoldshafen 76344, Germany
4. Department of Chemical Engineering and Materials Science, Michigan State University, East Lansing, Michigan 48824, USA

## **Corresponding Author**

\* Richard M. Laine. E-mail: [talsdad@umich.edu](mailto:talsdad@umich.edu)

**Abstract:** Biomass-derived materials offer low carbon approaches to energy storage. High surface area SiC w/wo 13 wt. % hard carbon (SiC/HC, SiC/O), derived from carbothermal reduction of silica depleted rice hull ash (SDRHA), can function as Li<sup>+</sup> battery anodes. Galvanostatic cycling of SiC/HC and SiC/O shows capacity increases eventually to >950 mAh g<sup>-1</sup> (Li<sub>1.2-1.4</sub>SiC) and >740 mAh g<sup>-1</sup> (Li<sub>1.1</sub>SiC), respectively, after 600 cycles. Post-mortem investigation via XRD and <sup>29</sup>Si MAS NMR reveal partial phase transformation from 3C- to 6H-SiC, with no significant changes in unit cell size. SEMs show cycled electrodes maintain their integrity, implying almost no volume expansion on lithiation/delithiation, contrasting with >300 % volume changes in Si anodes on lithiation. Significant void space is needed to compensate for these volume changes with Si in contrast to SiC anodes suggesting nearly competitive capacities. <sup>6</sup>Li MAS NMR and XPS show no evidence of Li<sub>x</sub>Si, with Li preferring all-C environments supported by computational modeling. Modeling also supports deviation from the 3C phase at high Li contents with minimal volume changes.

## 1. Introduction

The global momentum targeting new energy sources to tackle loss/replace traditional energy sources recognize that such measures must be coupled strongly to environmental concerns.<sup>1-3</sup> One crucial approach replaces traditional fuel-based with sustainable energy sources, especially next-generation lithium-ion batteries (LIBs) relying on non-graphitic anodes, e.g. silicon (Si).

A further mandate is to develop sustainable batteries.<sup>4,5</sup> Any environmental impact evaluation must sum energy output and input vis a vis chemical composition, battery materials syntheses, energy consumed in fabrication, implementation, and recycling.<sup>4-6</sup> To this end, heavy metal-containing active electrode materials generate significant greenhouse gas emissions during battery production and operation; a substantial component of “sustainability criteria”.<sup>7</sup>

Clearly, recycling spent LIBs is of great importance from the viewpoint of protecting resources and the environment. However, LIB recycling efforts focus mainly on valuable metals, e.g., cobalt, nickel, lithium, copper, etc. Research on recovery of graphite in spent LIBs is limited. Time- and energy-consuming purification processes are required to obtain battery-grade graphite from either synthetic or natural sources, including mining, beneficiation, impurity removal by HF treatment, graphitization to  $> 2500^{\circ}\text{C}$ , producing considerable  $\text{CO}_2$ ,  $\text{NO}_x$ ,  $\text{SO}_x$ , and particulate emissions.<sup>8-12</sup>

Moreover, graphite's theoretical capacity is only  $372 \text{ mAh g}^{-1}$ ,<sup>13,14</sup> and susceptibility to lithium plating limiting fast-charging are major obstacles to improving the performance of current LIBs.<sup>2,15</sup> In principle, Si's high capacity ( $3579 \text{ mAh g}^{-1}$ ),<sup>16-18</sup> great natural abundance and low toxicity make it an undisputed superior candidate to replace graphite anodes.<sup>13,14</sup> Unfortunately, the significant volume changes ( $\Delta V > 300 \%$ ) during  $\text{Li}^+$  alloying/dealloying and consequent poor capacity retention are fatal to commercial-scale use.<sup>14,19,20</sup> Multiple attempts to resolve these issues include fabrication of nanoscale Si-based materials<sup>20-22</sup> in various designed structures, as Si/C

composites,<sup>23–25</sup> and derivatives, including  $\text{SiO}_x$  as potential substitutes.<sup>18,26–28</sup> Some commercial graphite anodes mixed with small amounts (4–10 wt. %) of Si-containing materials have reached LIB markets.<sup>18,27</sup> Significant barriers to more efficient use of Si-based anodes remain.

Recently, silicon carbide's (SiC) potential as an anode material for LIBs has emerged. Si-C bilayer stacking offers a primary foundation for lithium intercalation. Kumari et al.<sup>29</sup> reported initial discharge capacities  $\approx 1330 \text{ mAh g}^{-1}$  with retained capacity  $\approx 1200 \text{ mAh g}^{-1}$  (200 cycles) using 50 nm-diameter SiC obtained by CVD of Si nanoparticles using methane. This initial report prompted further efforts to explore this traditionally electrochemically inactive material. Sun et al.<sup>30</sup> pyrolyzed resin-silica composites generating 3C-SiC nanofibers with 7.5 wt. % free carbon finding a discharge capacity of  $540 \text{ mAh g}^{-1}$  (500 cycles). Zhao et al.<sup>31</sup> synthesized C/SiC nanowire (dia. 8–10 nm) composites by electrolyzing carbonized rice hulls (RHs), finding capacities  $> 1000 \text{ mAh g}^{-1}$  ( $> 400$  cycles). Note that rice hulls with densities of  $< 0.15 \text{ g/cc}$  would mandate excessive capital equipment investment compared to RHA ( $> 1 \text{ g/cc}$ ) if their use were to be scaled for commercial applications.<sup>32</sup>

Thus, renewable, biowaste-based anodes that offer performance superior to graphite without Si's attendant problems coupled with easy recycling offer significant motivation to realize truly green and sustainable energy sources. Ideally, closed carbon cycles could be maintained in energy storage devices where  $\text{CO}_2$  generated from producing LIBs is returned photosynthetically to biomatter, in turn, used to manufacture batteries. In particular, rice hull ash (RHA), a byproduct of RHs combustion *for their fuel value*, consists typically of 80–90 wt. % amorphous  $\text{SiO}_2$  intimately mixed with unburned hard carbon (HC) at the nanoscale. RHA is considered an agricultural waste. Several earlier studies have explored using RHs or RHA in production of SiC, including our own, but almost always with an added carbon source and/or hazardous chemical treatments.<sup>33–35</sup>

We previously described a method of directly extracting  $\text{SiO}_2$  from RHA to produce silica depleted RHA (SDRHA) using an environmentally- and economically-friendly approach.<sup>36</sup> In principle, this approach valorizes RHA as a practical precursor to solar grade silicon (99.999 % pure);<sup>37</sup> high surface area fumed and precipitated silicas for vacuum insulation panels;<sup>38</sup> high-performance electrodes for hybrid  $\text{Li}^+$  supercapacitors;<sup>39</sup> and precursors for solid  $\text{Li}^+$  electrolytes.<sup>40</sup>

In particular, SDRHA with controllable  $\text{SiO}_2$ :HC ratios allows more efficient use of the intimately mixed nano- $\text{SiO}_2$  and HC as natural starting materials for carbothermal reduction to high surface area  $\text{SiC}$ ,  $\text{Si}_2\text{N}_2\text{O}$ , or  $\text{Si}_3\text{N}_4$ , *without need for external carbon sources*. Meanwhile, impurities commonly seen in biomass are concurrently eliminated via pre-purification of RHA and thereafter SDRHA using dilute acid and boiling water washes that provide starting materials with purities  $> 99.9\%$ .<sup>41</sup>

Here, we report that SDRHA derived  $\text{SiC}$  with HC ( $\text{SiC}/\text{HC}$ ) and after simply oxidizing HC ( $\text{SiC}/\text{O}$ ) as LIB anodes offer incremental capacity increases, reaching  $> 950$  and  $740 \text{ mAh g}^{-1}$  after 600 cycles, respectively. Post-mortem and computational modeling studies provide insight into the mechanisms whereby these  $\text{SiC}$ -based electrodes function with minimal volume change ( $\Delta V$ ) suggesting a possible alternative to Si.

## 2. Results & discussion

We recently reported a novel method of extracting  $\text{SiO}_2$  from RHA via the direct distillation of the spiroxiloxane  $[(\text{CH}_3)_2\text{C}(\text{O})\text{CH}_2\text{CH}(\text{O})\text{CH}_3]_2\text{Si}$  coincidentally providing SDRHA with control of final  $\text{SiO}_2$ :C mole ratios of 2:15-13:35. This finding enables the production of  $\text{SiC}$  via direct carbothermal reduction of RHA more rapidly and at lower temperatures than traditional methods

as our approach takes advantage of the natural nanoscale mixing of SiO<sub>2</sub> and carbon in RHA without adding carbon and tedious milling processes, as described elsewhere.<sup>41</sup>

Greyish products are obtained by heating SDRHA<sub>60</sub> (60 wt. % SiO<sub>2</sub>, SSA  $\approx$  360 m<sup>2</sup>/g) at 1450 °C/8 h/Ar containing  $\approx$  13 wt. % hard carbon, as shown in Figure **S1a** via isothermal TGA under O<sub>2</sub> (denoted as SiC/HC below). The XRD (Figure **S1b**) and FTIR (Figure **S1c**) both indicate the products are composed mainly of  $\beta$ -phase SiC, belonging to the cubic crystallographic system (3C).<sup>42</sup> It should be noted that the low-intensity peak at a lower angle than that of the (111) plane is ascribed to the presence of stacking faults (marked with \*). Stacking faults occur frequently in growing SiC whiskers along {111} planes, perpendicular to the SiC whisker growth direction.<sup>43</sup>

Diffraction peaks observed at  $\approx$  36 °, 42 °, 60 °, and 72 ° 2 $\theta$  are associated with diffraction from the (111), (200), (220), and (311) planes of 3C-SiC, respectively. Analysis using the Halder-Wagner method gives a lattice parameter of 4.3518(19) Å, close to reference 3C-SiC parameters (4.348 Å). The peak for the (111) lattice plane shows a stronger residual diffraction signal in comparison with the peak intensities of the reference 3C-SiC DB card (PDF 01-073-1708), suggesting a long axis in the <111> direction in the SiC structure. The peak intensity ratio of (200) to (111) plane is 5.25, while that for the reference pattern is 17.5. The significant difference in peak intensities is presumably due to more favored orientation along the (111) vs. (200) planes, resulting from competitive growth along the two directions. It is generally accepted that the surface energy of {111} planes in 3C-SiC is lower than other lattice planes, which leads to 3C-SiC whiskers growing preferentially along the <111> direction with lower formation energy.<sup>44,45</sup>

The Figure **S1d** SEM image reveals two distinct SiC morphologies: particles and whiskers, resulting from coinciding different reaction mechanisms during carbothermal reduction.<sup>46-49</sup> The BET specific surface area (SSA) is  $\approx$  204 m<sup>2</sup>/g for SiC/HC, and  $\approx$  42 m<sup>2</sup>/g SiC after oxidative

removal at 500 °C/1 h/O<sub>2</sub> (denoted as SiC/O below), per Figure **S2a** N<sub>2</sub> adsorption/desorption isotherms. The broad pore size distribution in SiC/HC (Figure **S2b**) peaks at 17-24 nm, with no peaks seen for SiC/O (Figure **S2c**). HC typically exhibits high cross-linking inducing formation of nanopores within the disordered structures, an inescapable factor for HC-based anodes.<sup>50</sup>

### 2.1. Electrochemical performance of SiC/HC and SiC/O

SiC was long regarded as electrochemically inert to Li<sup>+</sup> and as a matrix to strengthen composite electrodes to mediate charge/discharge volume changes.<sup>51–53</sup> However, recent pioneering studies<sup>29–31,54–58</sup> inspired us to assess SDRHA derived SiC anodes, especially because they are synthesized readily from sustainable materials. Figure **1a** presents cross-sectional SEMs of a representative SiC/HC anode. The active materials loading is  $\approx 1 \text{ mg cm}^{-2}$ , giving an areal capacity of  $\approx 0.75 \text{ mAh cm}^{-2}$ . Both SiC/HC and SiC/O half-cell electrodes were assembled with Li metal as the counter electrode.

Figure **1b** provides CV curves for SiC/HC cycled between 3 and 0.01 V at  $1 \text{ mV s}^{-1}$ . In the first cathodic sweep, peaks appear at  $\approx 1$  and  $\approx 0.72$  V attributable to two carbonate reductive decomposition steps as the SEI forms on the anode surface. These steps disappear in subsequent scans, indicating a stable SEI.<sup>59–61</sup> Two oxidation peaks appearing at  $\approx 0.2$  and  $\approx 1.2$  V in anodic scans of both SiC/HC and SiC/O (Figure **S3b**) can be ascribed to Li<sup>+</sup> extraction. The reduction peak intensity at  $\approx 1.2$  V is lower in the 2<sup>nd</sup> and 3<sup>rd</sup> sweeps, presumably due to slow lithiation. Long plateaus appear between 0-2 V in Figure **1c** SiC/HC charge/discharge curves of Figure **S3c** for SiC/O. Figure **S3a** differential capacity analyses offer peaks at  $\approx 0.2$  and  $\approx 1.2$  V, in agreement with the CV results.

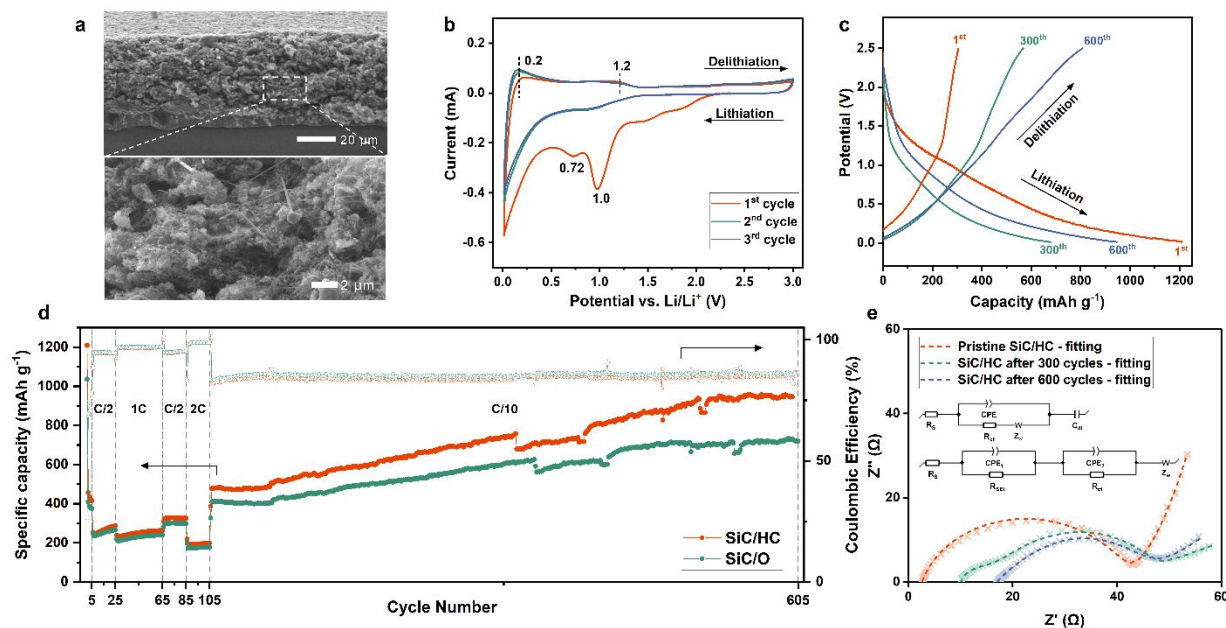


**Figure 1.** **a.** SEM images of cross-section of SiC/HC electrode, **b.** CV scanning curves of SiC/HC, **c.** charge/discharge curves of SiC/HC, **d.** specific capacity vs. cycle number of SiC/HC and SiC/O, and **e.** Nyquist plots (equivalent circuit model) of SiC/HC half cells before and after 300 and 600 cycles at 0.1C (inset: equivalent circuits).

Initial SiC/HC and SiC/O half-cell discharge capacities are  $\approx 1200$  and  $\approx 1040$  mAh g<sup>-1</sup>, respectively, indicating HC facilitates lithiation. However, initial Coulombic efficiencies (ICE) are both  $\approx 25$  %, with subsequent reversible discharge capacities of  $\approx 460$  and  $\approx 410$  mAh g<sup>-1</sup> for SiC/HC and SiC/O, respectively. The low ICEs can be ascribed to SEI formation and irreversible reactions.<sup>62–64</sup> The high SSAs of SiC/HC nanocomposites in the current work are likely responsible for high Li<sup>+</sup> consumption during initial cycles.<sup>65</sup>

Figure 1d plots galvanostatic cycling capacities of SiC/HC and SiC/O half-cells. The incremental increases in capacity with cycling are a distinctive feature of SiC electrodes. On cycling at C/2 for 20 cycles and 1C for 40 cycles, SiC/HC shows discharge capacities increase

from  $\approx 250$  to  $270 \text{ mAh g}^{-1}$  and  $\approx 230$  to  $280 \text{ mAh g}^{-1}$ , respectively. At 2C, capacities are  $\approx 200 \text{ mAh g}^{-1}$ . On cycling SiC/HC half-cells at C/10, discharge capacities reach  $\approx 950 \text{ mAh g}^{-1}$  (600 cycles). In comparison, HC-free SiC/O half-cells show discharge capacities  $\approx 20 \text{ mAh g}^{-1}$  lower at C/2-2C; but increases still occur. After 500 cycles at C/10, capacities reach  $\approx 740 \text{ mAh g}^{-1}$ .

Coulombic efficiencies (CE) for SiC/HC and SiC/O half-cells at C/10, C/2, 1C, and 2C are  $\approx 85$ , 95, 97, and 99 %, respectively. The relatively low CEs and high overpotential found for SiC/HC and SiC/O are nonideal for high-energy-density LIBs. Si-based anodes also exhibit poor later-cycle CEs from significant volume changes, particle pulverization, and repeated SEI reformation.<sup>66</sup> However, no previous literature discusses the origins of the typically low CEs for SiC-based anodes, as summarized in Table 1. Our studies offer some clues as to these processes, as discussed below. Optimizing CEs for SiC/HC and SiC/O anodes remains a subject for future studies.

**Table 1.** Electrochemical performance of reported SiC anode materials.

Materials	Synthesis method	Capacity (mAh g <sup>-1</sup> ) <sup>[a]</sup>	C rate	CE (%) <sup>[b]</sup>	Initial capacity (mAh g <sup>-1</sup> )	ICE (%)	Capacity increments	Ref
SiC	Commercial	443 (delithiation) after 200 c.	C/30	N/A	1537	41.1		29
SiC particle	Commercial	288 (lithiation) after 200 c.	0.1 A/g	> 90 *	884	48 *		64
C-coated SiC	CVD	1177 (delithiation) after 200 c.	C/30	N/A	2066	64.8		29
C-coated SiC	Pyrolysis	350 (lithiation) after 600 c.	0.6 A/g	N/A	480	31.25	√	62
SiC nanowire	CVD	397 (delithiation) after 100 c.	C/10	94	3000	16.7 *	√	56

SiC nanowire	Electro-deoxidation	720 (lithiation) after 100 c.	0.5 A/g	99.4	2266	45.5 *		55
rod-like SiC	Carbothermal reduction	400 (lithiation) after 500 c.	0.05 A/g	> 90 *	180	77.8 *	√	31
SiC/C nanotubes	Resin/silica pyrolysis	527 (lithiation) after 250 c.	0.1 A/g	96	824	22	√	67
SiC nanofiber/C	Resin/silica pyrolysis	540 (lithiation) after 500 c.	0.3 A/g	97	309	71.7	√	30
SiC nanowire/C	Molten salt electrolysis	1120 (lithiation) after 600 c.	0.5 A/g	99	1235	65	√	31
SiC thin film	PECVD	310 (delithiation) after 60 c.	C/5	N/A	210	89	√	58
SiC thin film	ICPCVD	376 (lithiation) after 100 c.	C/3	98	1595	86		54
SiC nanoshell @ hollow graphite	Sol-gel pyrolysis and	1345 (lithiation) after 600 c.	0.6 A/g	> 90 *	1944	36 *	√	62
epitaxial graphene @ SiC	Pressure pyrolysis	968 (lithiation) after 200 c.	0.1 A/g	> 90 *	2051	63.4 *		64
SiC/O	RHA	741 (lithiation) after 600c	C/10	85	1040	26	√	This work
SiC/HC composite	carbothermal reduction	959 (lithiation) after 600c.	C/10	85	1200	25	√	

[a] Results listed in the table were tested in half-cells. Values in parentheses indicate the number of cycles (c.) to reach the capacities. [b] Values marked by \* were read from figures as they were not specified in corresponding literature.

Key comparisons with the SiC electrodes listed in Table 1 indicate SDRHA derived SiC/HC composites: (1) retain relatively higher capacities vs. other reported materials; (2) are readily produced by “low-temperature” (1450 °C) carbothermal reduction of an agricultural waste that is

often land-filled yet can now be used perhaps at commercial levels; (3) RHA is a byproduct of RH combustion coincidentally generating 200 gigawatts and 200k tons RHA/year in the U.S. alone.<sup>68</sup> Given that the rice crop fixes CO<sub>2</sub>, this process is at least carbon neutral. It may be carbon negative if land-filled RHA generates CH<sub>4</sub>/CO<sub>2</sub> subsequently released to the atmosphere.

To further understand the performance of SiC/HC anodes, electrochemical impedance spectra (EIS) were run before and after cycling. In the Figure **1e** Nyquist plots, pristine SiC/HC shows one semicircle at high-to-middle frequency ranges from charge transfer resistance ( $R_{ct}$ ), while the lower intercept relates to the interphase resistance ( $R_s$ ), including ionic resistance of the electrolyte, the intrinsic resistance of the active materials and the contact resistance between the anode material and the current collector.<sup>69,70</sup> The tail in the low-frequency portion towards a vertical line where the imaginary part of impedance rapidly increases, which is a characteristic of capacitive behavior of ion diffusion due to the presence of HC in the electrode,<sup>71,72</sup> which exhibits a  $\approx 45^\circ$  linear Warburg resistance diffusion drift after cycling.

Corresponding equivalent circuit fitting (inset Figure **1d**) is consistent with experimental results. Accordingly,  $R_s$  for SiC/HC electrodes before and after 300 and 600 cycles are calculated as  $\approx 3$ , 10, and 36  $\Omega$ , while the  $R_{ct}$  values  $\approx 39$ , 30, and 24  $\Omega$ , respectively. These suggest improved charge transfer within SiC/HC composites as the electrode is activated and increased lithium contents from irreversible conversion and/or lithium plating resulting in subsequent loss of contact between active materials on cycling, which correlates with the relatively low CEs. Nevertheless, SiC/HC after 300 and 600 cycles exhibits an additional semicircle at high-frequency, corresponding to a stable  $R_{SEI}$  of  $\approx 4.5 \Omega$ .

The SiC/O electrode was used for galvanostatic intermittent titration technique (GITT) assessment to eliminate HC effects.<sup>73</sup> The Li<sup>+</sup> diffusion coefficients (D) run  $10^{-22}$  -  $10^{-14}$  cm<sup>2</sup> s<sup>-1</sup>, per Figure S4, which decrease at higher SOCs, maximizing at  $\approx 14$  % lithiation (discharge) presumably attributable to reduced potential differences and fewer occupied sites that deactivate ion transport.<sup>74,75</sup>

## 2.2. Lithiation mechanisms

As discussed above, although incremental capacity increases were observed previously, their origins remain controversial. Reported explanations include (1) crystal structure transformation arising from Li<sup>+</sup> intercalation; (2) displacement reactions typical of conversion reactions resulting in slow formation of Si, C, and/or LiSi<sub>x</sub>C<sub>y</sub>; (3) slow and complex SEI formation.<sup>64</sup> To further investigate SiC lithiation mechanisms, post-mortem studies were conducted after 600 cycles.

Recovered electrodes were first cleaned (see experimental). Figure 2a compares XRDs of SiC/HC before/after cycling. The broad hump centered  $\approx 25^\circ 2\theta$  in cycled SiC/HC is ascribed to amorphous carbon used in electrodes. In addition to peaks assigned to 3C-SiC, XRDs of cycled SiC/HC exhibit weak peaks at  $\approx 38^\circ$ ,  $41^\circ$ ,  $44^\circ$ ,  $55^\circ$ ,  $64^\circ$ , and  $75^\circ 2\theta$ , corresponding to (103), (104), (105), (107), (109), (204) planes of 6H-SiC, respectively. Lattice parameters for 3C-SiC increase from 4.3518(19) to 4.3533(6) Å after 600 cycles, possibly indicating slight structural changes.

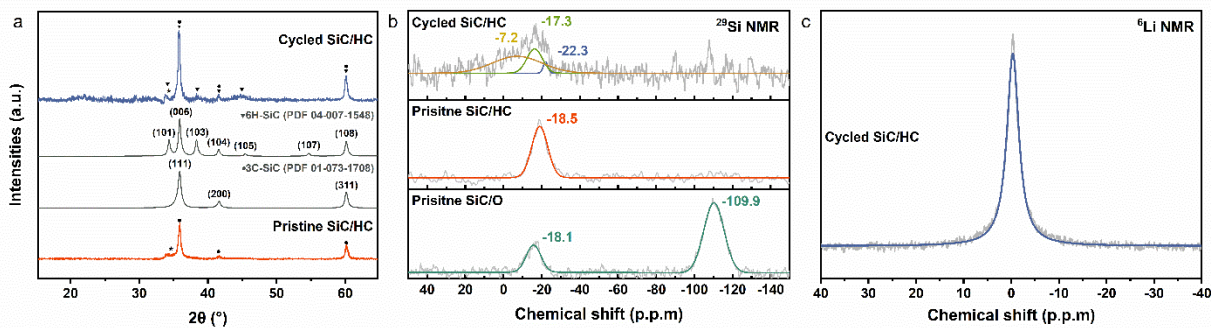


**Figure 2.** a. XRD of pristine and cycled SiC/HC, b.  $^{29}Si$  MAS NMR spectra of cycled SiC/HC compared with pristine SiC/HC and SiC/O, and c.  $^6Li$  MAS NMR spectra of cycled SiC/HC.

SiC polytype transformation during charge/discharge was observed by Kumari et al.,<sup>29</sup> who found 8H-SiC after cycling 3C-SiC nanoparticles. They suggest this transformation is related to the incremental capacity increases. Subsequently, Li et al.<sup>62</sup> describe 3C-SiC nanoshell transformation to 6H-SiC in encapsulated, hollow graphite spheres. DFT calculations by Bijoy et al.<sup>76</sup> suggest formation of an intermediate planar structure during polytype transformation.

More definitive analytical efforts appear necessary to better resolve these unresolved issues. Thus,  $^{29}Si$  and  $^6Li$  MAS NMR studies were run to identify surface and bulk structural changes. The Figure 2b  $^{29}Si$  NMR of pristine SiC/HC shows a strong peak for 3C-SiC at -18.5 ppm,<sup>77</sup> consistent with XRD and FTIR results. An additional peak found in the SiC/O samples centered at -109.9 ppm is associated with amorphous  $SiO_x$ ,<sup>78-80</sup> originating from oxidative removal of HC.

After cycling, the  $^{29}Si$  signal broadens, likely from structural disorder arising during lithiation/delithiation.<sup>81</sup> Deconvoluting this broad peak by Gaussian fitting finds two additional peaks. 6H-SiC typically shows peaks at -20 ~ -22 ppm, -14 ~ -17 ppm, and -25 ~ -27 ppm in  $^{29}Si$  spectra.<sup>78,82</sup> Thus, the fitted peak at -22.3 ppm is assigned to hexagonal SiC and/or intermediate phases. Insufficiently delithiated Si electrodes are reported to also show broadened  $^{29}Si$  peaks, reflecting distributions of local environments.<sup>83</sup> The broad peak at -7.2 ppm suggests irreversible-

lithiation of SiC and/or amorphization during lithiation/delithiation. In addition, the  $^6\text{Li}$  MAS NMR of lithiated SiC/HC generates a broad peak  $\approx -0.3$  ppm (Figure 2c), suggesting  $\text{Li}^+$  is located in an amorphous phase with a strong diamagnetic environment, typical of carbon environments.<sup>84,85</sup> These results are common to cycled electrodes due to SEI formation. There is no evidence for formation of well-crystallized  $\text{Li}_x\text{Si}$  or  $\text{Li}_x\text{C}$  phases.

Electrode surface changes were studied using XPS, as presented in Figure 3. Pristine SiC/HC and SiC/O show major peaks at 98, 153, 284, and 528 eV corresponding to Si 2p, Si 2s, C 1s, and O 1s, respectively. A small F 1s peak ascribed to the PVDF binder used in electrode fabrication appears at  $\approx 690$  eV. In cycled electrodes, the Si peaks are almost negligible, indicating the formation of an SEI layer. Table S1 records the quantitative analyses from XPS survey scan of SiC electrodes before and after cycling.

The stronger F 1s peak and coincident P 2p peak in cycled electrodes can be ascribed to  $\text{LiPF}_6$  electrolyte decomposition. It should be noted that the slight P 2p shift to lower binding energy (BE) from pure  $\text{LiPF}_6$  (138.2 eV) is often observed for small amounts of lithium salts at electrode surfaces due to XPS differential charging effects induced by insulating species at the surfaces.<sup>86,87</sup>

The C 1s core spectra presented in Figure 3b indicate both pristine SiC/HC and SiC/O electrodes show mainly deconvoluted peaks of C-Si, while C=C and C-O from the conductive additives, as summarized in Table S2. Peaks at 290 eV ( $\text{CF}_2$ ) and the wide 287-290 eV peak are visible in C 1s core spectra of both cycled SiC/HC and SiC/O electrodes, originating from the SEI surface.

Deconvolution analyses of the Si 2p core spectra in Figure 3c reveal Si-C (100.9 eV) and C-O-Si (100.3 eV) bonds in the pristine SiC/HC electrode, while the small, broad peak at  $\approx 99$  eV in Si 2p core spectra can be attributed to irreversible amorphous  $\text{LiSi}_x\text{C}_y$  species in cycled electrodes. Pristine SiC/O also shows a peak at 102.9 eV assigned to  $\text{SiO}_x$  ( $x \leq 2$ ). No Si core level peak was

observed in cycled SiC/O electrodes, presumably due to the relatively higher amounts of decomposed components on the surface, as suggested in the C 1s spectra. The Li 1s spectra of both cycled electrodes show a peak at  $\approx 56.5$  eV associated with LiF,  $\text{Li}_x\text{PF}_y$ ,  $\text{Li}_x\text{PF}_y\text{O}_z$ , and Li-bearing organics.<sup>88</sup> However, no peaks appear for elemental Si,  $\text{Li}_x\text{Si}$ , or  $\text{Li}_x\text{C}$  in either spectrum, agreeing with MAS NMR observations.

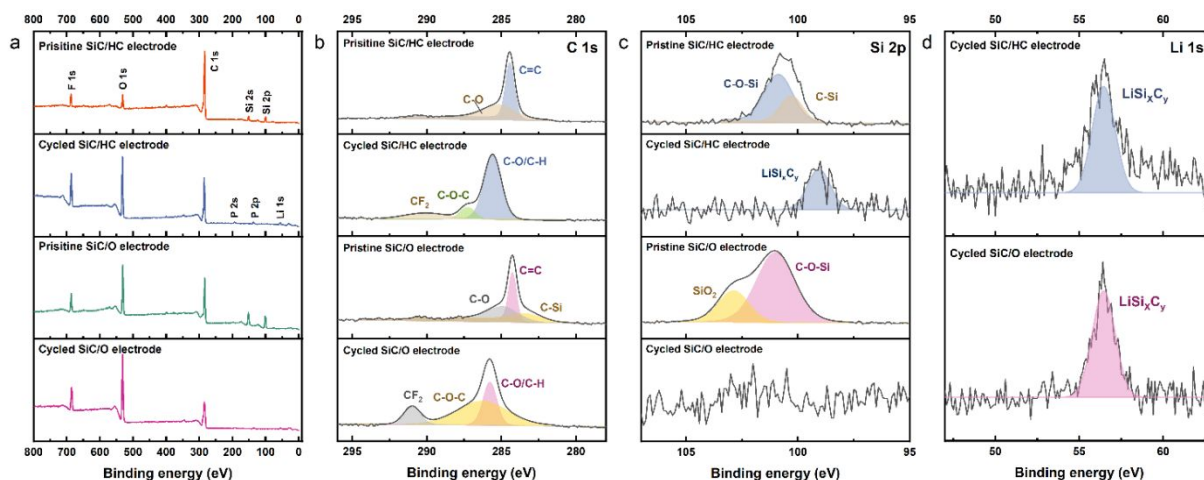


**Figure 3.** a. Wide-scan survey XPS spectra, b. C 1s c. Si 2p, and d. Li 1s core level spectra of SiC/HC and SiC/O electrodes before and after 600 cycles.

Figure 4 SEMs present microstructures of pristine and cycled SiC/HC and SiC/O electrodes, both consisting of larger (2-10  $\mu\text{m}$ ) particles after 600 cycles, indicating stable and robust SEI layers remain on extended cycling. Whiskers also remain, although are not dominant features. Overall, the electrodes maintain their integrity without significant volume changes on aging, suggesting the cubic to hexagonal phase transition does not alter the initial SiC electrode structure and/or morphology. EDX mapping in Figure S5 shows uniformly distributed Si, C, O, and F in pristine electrodes and P after cycling, supporting the XPS analyses.

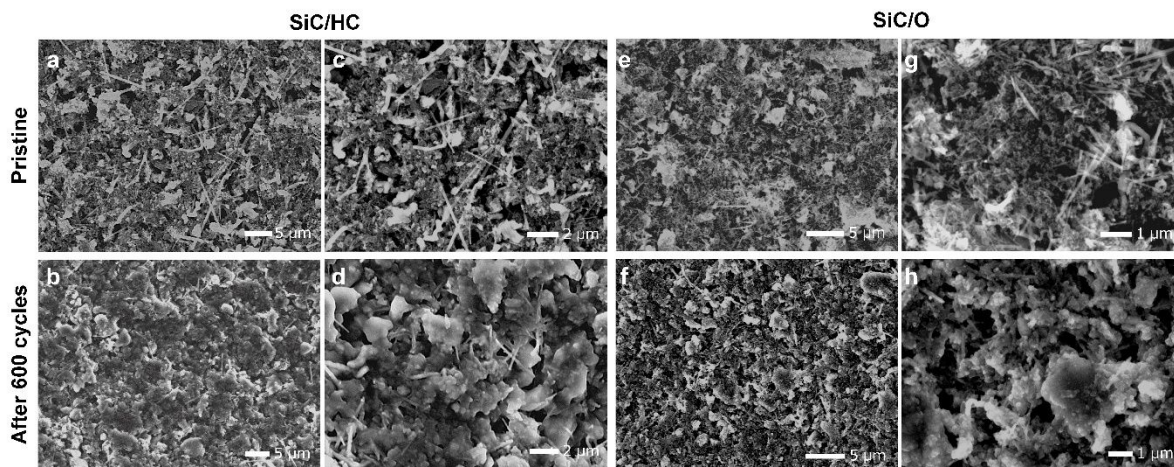


**Figure 4.** SEM images of **a.** pristine, **b.** cycled SiC/HC electrodes, **c.** pristine, and **d.** cycled SiC/O electrodes.

These results contrast greatly with Si electrodes, which suffer from pulverization and shortened cycle lives due to the high  $\Delta V$  during cycling.<sup>14,66</sup> Highly precise measurements of volume changes are undoubtedly valuable and likely require *in operando analyses*; best done after further optimization of current materials.

Nevertheless, modeling provides additional insight into the lithiation mechanism. To model lithiation of 3C-SiC, 4, 8, and 16 Li atoms were initially placed at the tetrahedral interstitial sites of either Si (named as Si-Td) or C (C-Td), in the supercell with 32 Si and 32 C atoms. Analysis of MD trajectories suggest that Li prefers to stay at C-Td: if Li atoms were initially at placed at Si-Td, they move to C-Td; if Li atoms were initially at C-Td, they would stay there, and no diffusion could be detected within 13 ps at 1200 K. This slow Li diffusion is consistent with the experimental observation of improved capacities on long-term cycling of SiC electrodes, explaining the relatively high overpotential needed to overcome the initial activation energy barrier.

In addition, MD simulations suggest that  $\text{Li}_x\text{SiC}$  maintains the cubic phase at  $x=0.125$  and  $0.25$ , deviating from cubic at  $x=0.5$ . This phase transformation may explain the higher than theoretical capacity observed experimentally.

Easily oxidized SiC surfaces always contain Si-O species,<sup>89</sup> reflected in MAS NMR and XPS. In principle,  $\text{SiO}_x$  species can also contribute to capacities via  $2x \text{Li} + \text{SiO}_x \rightarrow x \text{Li}_2\text{O} + \text{Si}$  and subsequent alloying/dealloying reactions.<sup>90</sup>

However, the characterization data are absent elemental Si or amorphous  $\text{Li}_x\text{Si}$ , suggesting minimal  $\text{SiO}_x$  contributions. The SiC/O oxidized surfaces likely provide a second explanation for the differences observed and the SiC modeled here.<sup>91-93</sup> However, the  $950 \text{ mAh g}^{-1}$  value for SiC/HC requires further consideration. HC lithiation mechanisms are unclear, with capacities depending largely on the degree and type of disorder.<sup>94</sup> It is widely accepted that HC exhibits specific capacities of  $500\text{--}700 \text{ mAh g}^{-1}$  after heat-treating at  $\approx 1000 \text{ }^\circ\text{C}$ , while heating  $> 1000 \text{ }^\circ\text{C}$  promotes graphene sheet growth lowering capacities to  $< 200 \text{ mAh g}^{-1}$ .<sup>95,96</sup> Accordingly, if HC contributes to this capacity, 13 wt. % HC would contribute no more than  $\approx 20\text{--}90 \text{ mAh g}^{-1}$ ; thus,  $\approx 160\text{--}230 \text{ mAh g}^{-1}$  remains unaccounted for but likely arises from interfaces between 3C- and 6H-SiC, or also from stacking faults.

One reasonable conclusion is that this system lithiates to form a material with  $\text{Li}_{1.2-1.4}\text{SiC}$ . This has important implications about realistic SiC anode vs. Si-based anodes capacities; see below.

### 3. Conclusions

SiC/HC and SiC/O nanocomposite anodes derived from RHA are potential alternatives to graphite and competitors to Si anodes in future LIBs. SiC/HC undergoes incremental capacity

increases to  $> 950 \text{ mAh g}^{-1}$  after 600 cycles with ambient  $\text{Li}^+$  diffusion coefficients of  $10^{-22} - 10^{-14} \text{ cm}^2 \text{ s}^{-1}$  as measured by GITT.

Post-mortem characterization of cycled electrodes using XRD,  $^{29}\text{Si}$  NMR, XPS, and SEM indicate partial phase transformation from cubic (3C) to hexagonal (6H) SiC, with no significant volume changes or surface cracking observed in SEMs. No elemental Si,  $\text{Li}_x\text{Si}$ , or  $\text{Li}_x\text{C}$  is observed, suggesting SiC lithiation is limited by intercalation rather than conversion or alloying reactions. Computational modeling suggests that a cubic to hexagonal phase transition occurs at high Li contents and indicates that Li prefers the tetrahedral C site due to electrostatic interactions.

Experimental data indicate that lithiated SiC reaches a composition of  $\text{Li}_{1.2-1.4}\text{SiC}$  without significant volume changes resulting in capacities approaching  $\approx 1000 \text{ mAh g}^{-1}$ . Thus SiC may offer a realistic alternative to Si. The arguments in favor of this conclusion come from the fact that lithiation of Si to  $\text{Li}_{4.4}\text{Si}$  occurs with  $\Delta V > 300 \%$ , meaning that cells with Si anodes must accommodate a significant fraction of this volume change.

This allows the conclusion (disregarding mechanical properties issues) that, due to the required  $\approx 40\text{-}60 \%$  void space needed in a host material, the actual capacity of a realistic Si-based anode would be half of 3579 or 1300  $\text{mAh g}^{-1}$  at best. A recent study reported mesoporous Si films made from wafer sawed single crystals showing specific capacities of  $1200 \text{ mAh g}^{-1}$  for 450 cycles<sup>97</sup> offering justification for our estimate. Additionally, SiC could eliminate surface protection needed for Si-based anodes in part as well. At this point, SiC becomes competitive.

There are clear challenges to making SiC a truly viable anode material, including fully understanding the open circuit potential, learning to optimize the overpotential and speed capacity

increases such that one can reach feasible capacities in many fewer than 600 cycles, and demonstrating the realistic utility of SiC in full-cell formats.

A further point to be made is that because one can start from RHA, an agricultural waste available in 200k tons/year (U.S. alone) and which allows production of SiC/HC and SiC/O (> 99.9 % pure) at temperatures of 1400-1500 °C (much lower than typical carbothermal reductions) and much lower than used to produce graphite and metallurgical grade Si even from SDRHA. It may also be possible to use energy generated by RH combustion, allowing a true carbon neutral approach. *Finally, SiC is an extremely hard material that could have a second life simply as an abrasive offering at least one option for facile recycling.*

## 4. Material and Methods

### 4.1. Synthesis of SiC from silica-depleted rice hull ash (SDRHA)

The detailed extraction of SiO<sub>2</sub> from RHA (Wadham Energy Inc.) to recover SDRHA and distill spiroxiloxane was reported elsewhere.<sup>36,98,99</sup> Synthesis of SiC via carbothermal reduction of the SDRHA with various SiO<sub>2</sub>:C ratios was detailed recently.<sup>41</sup> In brief, (60 wt. % SiO<sub>2</sub>) powders were placed in a covered graphite crucible. On heating at 1450 °C/8 h/10 °C/min/Ar produces SiC/HC (≈ 85/15). The excess hard carbon can be removed by oxidizing at 500 °C/1 h/O<sub>2</sub>.

### 4.2. SiC half-cell assembly

SiC/HC and SiC/O electrodes were prepared with 70 wt. % SiC/HC or SiC/O, 20 wt. % C<sub>65</sub>, and 10 wt. % poly(vinylidene fluoride) (PVDF) binder. SiC powders and C<sub>65</sub> were dried at 80 °C/vacuum overnight and dry-mixed by mortar and pestle, which was then mixed with PVDF binder solution (5 wt. % solution in NMP) and 1.5 g NMP in a 16 mL vial. The mixtures were

ball-milled with yttria-stabilized zirconia media (3 mm dia.) overnight to obtain uniform slurries, then coated onto a copper foil (16  $\mu\text{m}$  thick) using a wire-wound rod coater at a controlled speed of 50 mm/s. After drying at 80  $^{\circ}\text{C}$ /vacuum/2 h, 18 mm dia. electrodes were punched out. SiC anode porosities were calculated by:  $1 - \left( \frac{0.7 \times m}{\rho_{\text{active}}} + \frac{0.1 \times m}{\rho_{\text{C}_{65}}} + \frac{0.2 \times m}{\rho_{\text{PVDF}}} \right) / (S \times H)$ , where  $m$  is the total mass coated on current collector,  $\rho_{\text{active}}$ ,  $\rho_{\text{C}_{65}}$  and  $\rho_{\text{PVDF}}$  are the densities of active materials (SiC, 3.21  $\text{g cm}^{-3}$ ), super C<sub>65</sub> carbon black (1.6  $\text{g cm}^{-3}$ ) and PVDF (1.78  $\text{g cm}^{-3}$ ), respectively.  $S$  is the area of electrode, and  $H$  is the thickness of the coating on the current collector.

Half-cells (2023 coin cell) were assembled with SiC/HC and SiC/O electrodes, with Li metal used as the counter electrode in a glovebox. The metallic Li (16 mm  $\times$  750  $\mu\text{m}$ , Alfa Aesar) was scraped to remove the oxide layer and expose a clean surface before cell assembly. Celgard 2400 (19 mm) was used as a separator and 1.1 M LiPF<sub>6</sub> in EC:DC:DMC (1:1:1 weight ratio) with 10 wt. % FEC additive as the electrolyte.

### 4.3. Material Characterization

Fourier-transform infrared spectroscopy (FTIR) Nicolet 6700 Series FTIR spectrometer (Thermo Fisher Scientific, Inc.) was used to collect FTIR spectra. X-ray diffraction (XRD, Rigaku Miniflex) was measured with Cu-K $\alpha$  radiation ( $k = 0.154 \text{ nm}$ ) in the  $2\theta$  over the ranges of 10-80 $^{\circ}$   $2\theta$  to identify the crystallinity nature and phases. Micromeritics ASAP 2020 sorption analyzer was used for BET specific surface area (SSA) analyses. Samples were degassed at 300  $^{\circ}\text{C}$ /6 h prior to analyses by N<sub>2</sub> physisorption at -196  $^{\circ}\text{C}$  (77 K). BET method using 10 data multipoint with relative pressures of 0.05-1 was applied. The pore volume was calculated based on the Barret–Joyner–Halenda (BJH) model. JSM-IT300HR In Touch Scope SEM (JEOL USA, Inc.) was used to acquire the microstructure images and EDX maps. Q600 simultaneous TGA/DSC (TA Instruments, Inc.) was used for thermogravimetric analysis (TGA). Magic-angle spinning (MAS) nuclear magnetic

resonance (NMR) spectroscopy  $^6\text{Li}$  and  $^{29}\text{Si}$  magic-angle spinning (MAS) nuclear magnetic resonance (NMR) spectroscopy was performed with a Bruker Avance 500 MHz spectrometer at a magnetic field of 11.7 T, corresponding to resonance frequencies of 73.6 and 99.4 MHz, respectively. Spinning was performed in 2.5 mm rotors at 30 kHz. Spectra were acquired with a  $\pi/2$  pulse duration of 2.8  $\mu\text{s}$  for  $^6\text{Li}$  and 1.8  $\mu\text{s}$  for  $^{29}\text{Si}$ , and a recycle delay of 30 s for  $^6\text{Li}$  and 60 s for  $^{29}\text{Si}$ . X-ray photoelectron spectroscopy (XPS) was done using the Kratos Axis Ultra (Kratos Analytical) at room temperature under  $3.1 \times 10^{-8}$  Pa using monochromatic Al source (14 kV and 8 mA) to record the core level atoms. The binding energies of all the elements were calibrated relative to C 1s at 284.8 eV.

#### 4.4. Electrochemical measurements

Data shown in the article was averaged of three cells. The galvanostatic cycling of the half-cells was performed between 0.01 - 2.5 V vs. Li/Li<sup>+</sup> using a multi-channel Maccor test system. The experimental mole of Li in lithiated SiC was calculated per  $n_{\text{Li}} = Q_{\text{experimental}}/F \times M_{\text{SiC}}$ , where F is the Faraday constant, and  $M_{\text{SiC}}$  is 40.096 g/mol.

A Bio-Logic SP-300 was used to measure the open-circuit voltage, the AC impedance, cyclic voltammetry (CV), and galvanostatic intermittent titration technique (GITT). The EIS data was recorded in a frequency range of 7 MHz to 1 Hz with an AC amplitude of 10 mV. The CV tests were conducted in the range of 0.01-3 V with a scan rate of 0.1 mV/s. The GITT tests were applied to the half-cells between 0.01 - 3 V at a 0.1 C rate for 10 minutes, followed by resting periods of 20 min. The potential change of the current pulse vs. the square root of time ( $\tau^{1/2}$ ) exhibits linear behavior with  $R^2$  of  $\approx 0.91$  (Figure S4b).<sup>100,101</sup> The ion diffusion coefficient (D) was calculated per

$D = \frac{4}{\pi\tau} \left( \frac{n_M \times V_M}{A_e} \right)^2 \left( \frac{\Delta E_S}{\Delta E_\tau} \right)^2$  where  $n_M$  is the moles of active material,  $A_e$  is the contact area between the

electrolyte and electrode,  $\Delta E_S$  is the steady-state voltage change, and  $\Delta E_\tau$  is the voltage change after eliminating the IR drop during the constant current pulse.<sup>73,100,102</sup>

The SiC/HC and SiC/O half-cells after completing the 600 cycles test were decrimped in a dry room. The recovered electrodes were rinsed and soaked in DEC solvent to remove electrolyte salt residues that are not inherent to the SEI prior to dissolving the PDVF binder in NMP using ultrasonication. The electrodes were then dried overnight under vacuum at room temperature. The coatings on the SiC electrodes after cycling for 600 cycles were also scraped from the current collector using a razor blade in a dry room to gain better resolution active materials with eliminating the detection of Cu in following characterization.

#### **4.5. Modeling**

Density-functional theory based molecular dynamics (DFT-MD) simulations under the isobaric-isothermic ensemble were performed by the VASP package utilizing the Projector Augmented-Wave (PAW) method.<sup>103,104</sup> DFT calculations were performed with the PBEsol exchange-correlation functional,<sup>105</sup> a plane-wave cutoff energy of 550 eV, and a single k (Gamma) point. MD simulations were performed for 13 ps at an elevated temperature of 1200 K, in order to accelerate the dynamics. Atomic charges and bond orders were in the DDEC6 scheme.<sup>106</sup> The supercell of 3C-SiC contains 64 atoms.

#### **5. Conflicts of interest**

There are no conflicts to declare.

#### **6. Acknowledgments**

We acknowledge supports from DMR NSF Grant No. DMR-1926199 and a generous gift from Mercedes-Benz Research & Development North America (MBRDNA) for this work. We appreciate the advice provided by Dr. Gregory Less at the University of Michigan Battery Lab, and the technical support from Van Vlack lab and Michigan Center for Materials Characterization. We also thank the gift of rice hull ash from Wadham Energy Inc. and Clara Huang's assistance on SDRHA synthesis.

## References

- 1 V. Pellegrini, S. Bodoardo, D. Brandell and K. Edström, *Solid State Communications*, 2019, **303–304**, 113733.
- 2 Y. Liu, Y. Zhu and Y. Cui, *Nature Energy*, 2019, **4**, 540–550.
- 3 A. Tomaszewska, Z. Chu, X. Feng, S. O'Kane, X. Liu, J. Chen, C. Ji, E. Endler, R. Li, L. Liu, Y. Li, S. Zheng, S. Vetterlein, M. Gao, J. Du, M. Parkes, M. Ouyang, M. Marinescu, G. Offer and B. Wu, *eTransportation*, 2019, **1**, 100011.
- 4 C. Liedel, *ChemSusChem*, 2020, **13**, 2110–2141.
- 5 D. Larcher and J.-M. Tarascon, *Nature Chemistry*, 2015, **7**, 19–29.
- 6 S. Dühnen, J. Betz, M. Kolek, R. Schmuch, M. Winter and T. Placke, *Small Methods*, , DOI:10.1002/smtd.202000039.
- 7 M. Romare and L. Dahllöf, 58.
- 8 C. Liang, Y. Chen, M. Wu, K. Wang, W. Zhang, Y. Gan, H. Huang, J. Chen, Y. Xia, J. Zhang, S. Zheng and H. Pan, *Nature Communications*, 2021, **12**, 119.
- 9 O. Fromm, A. Heckmann, U. C. Rodehorst, J. Frerichs, D. Becker, M. Winter and T. Placke, *Carbon*, 2018, **128**, 147–163.
- 10 J. Peng, N. Chen, R. He, Z. Wang, S. Dai and X. Jin, *Angewandte Chemie International Edition*, 2017, **56**, 1751–1755.
- 11 A. D. Jara, A. Betemariam, G. Woldetinsae and J. Y. Kim, *International Journal of Mining Science and Technology*, 2019, **29**, 671–689.

- 12 I. Rey, C. Vallejo, G. Santiago, M. Iturrondobeitia and E. Lizundia, *ACS Sustainable Chem. Eng.*, 2021, **9**, 14488–14501.
- 13 J. Lu, Z. Chen, F. Pan, Y. Cui and K. Amine, *Electrochem. Energ. Rev.*, 2018, **1**, 35–53.
- 14 A. Franco Gonzalez, N.-H. Yang and R.-S. Liu, *J. Phys. Chem. C*, 2017, **121**, 27775–27787.
- 15 Q. Liu, C. Du, B. Shen, P. Zuo, X. Cheng, Y. Ma, G. Yin and Y. Gao, *RSC Adv.*, 2016, **6**, 88683–88700.
- 16 H. Yang, C. Guo, A. Naveed, J. Lei, J. Yang, Y. Nuli and J. Wang, *Energy Storage Materials*, 2018, **14**, 199–221.
- 17 B. Zhu, X. Wang, P. Yao, J. Li and J. Zhu, *Chemical Science*, 2019, **10**, 7132–7148.
- 18 M. Ko, S. Chae, J. Ma, N. Kim, H.-W. Lee, Y. Cui and J. Cho, *Nature Energy*, 2016, **1**, 1–8.
- 19 J. R. Szczech and S. Jin, *Energy & Environmental Science*, 2010, **4**, 56–72.
- 20 X. Su, Q. Wu, J. Li, X. Xiao, A. Lott, W. Lu, B. W. Sheldon and J. Wu, *Advanced Energy Materials*, 2014, **4**, 1300882.
- 21 M. Ashuri, Q. He and L. L. Shaw, *Nanoscale*, 2015, **8**, 74–103.
- 22 K. Eom, T. Joshi, A. Bordes, I. Do and T. F. Fuller, *Journal of Power Sources*, 2014, **249**, 118–124.
- 23 Yolk-shell Si/SiO<sub>x</sub>@Void@C composites as anode materials for lithium-ion batteries | Functional Materials Letters, <https://www.worldscientific.com/doi/abs/10.1142/S1793604718500947>, (accessed October 16, 2019).
- 24 R. Yi, F. Dai, M. L. Gordin, S. Chen and D. Wang, *Advanced Energy Materials*, 2013, **3**, 295–300.
- 25 M. Xia, Y. Li, Y. Wu, H. Zhang, J. Yang, N. Zhou, Z. Zhou and X. Xiong, *Applied Surface Science*, 2019, **480**, 410–418.
- 26 Z. Liu, Q. Yu, Y. Zhao, R. He, M. Xu, S. Feng, S. Li, L. Zhou and L. Mai, *Chem. Soc. Rev.*, 2019, **48**, 285–309.
- 27 H. Wang, J. Fu, C. Wang, J. Wang, A. Yang, C. Li, Q. Sun, Y. Cui and H. Li, *Energy Environ. Sci.*, 2020, **13**, 848–858.
- 28 J. Yang, Y. Takeda, N. Imanishi, C. Capiglia, J. Y. Xie and O. Yamamoto, *Solid State Ionics*, 2002, **152–153**, 125–129.
- 29 T. S. D. Kumari, D. Jeyakumar and T. P. Kumar, *RSC Adv.*, 2013, **3**, 15028–15034.

- 30 X. Sun, C. Shao, F. Zhang, Y. Li, Q.-H. Wu and Y. Yang, *Front. Chem.*, , DOI:10.3389/fchem.2018.00166.
- 31 Z. Zhao, H. Xie, J. Qu, H. Zhao, Q. Ma, P. Xing, Q. Song, D. Wang and H. Yin, *Batteries & Supercaps*, 2019, **2**, 1007–1015.
- 32 B. Singh, in *Waste and Supplementary Cementitious Materials in Concrete*, eds. R. Siddique and P. Cachim, Woodhead Publishing, 2018, pp. 417–460.
- 33 J. Xia, N. Zhang, S. Chong, D. Li, Y. Chen and C. Sun, *Green Chem.*, 2018, **20**, 694–700.
- 34 K. Sujirote and P. Leangsuwan, *Journal of Materials Science*, 2003, **38**, 4739–4744.
- 35 C. Real, M. D. Alcalá and J. M. Criado, *Journal of the American Ceramic Society*, 2004, **87**, 75–78.
- 36 R. M. Laine, J. C. Furgal, P. Doan, D. Pan, V. Popova and X. Zhang, *Angewandte Chemie*, 2016, **128**, 1077–1081.
- 37 J. C. Marchal, D. J. Krug, P. McDonnell, K. Sun and R. M. Laine, *Green Chemistry*, 2015, **17**, 3931–3940.
- 38 C. D. Li, M. U. Saeed, N. Pan, Z. F. Chen and T. Z. Xu, *Materials and Design*, , DOI:10.1016/j.matdes.2016.06.071.
- 39 E. Temeche, M. Yu and R. M. Laine, *Green Chemistry*, 2020, **22**, 4656–4668.
- 40 X. Zhang, E. Temeche and R. M. Laine, *Green Chemistry*, 2020, **22**, 7491–7505.
- 41 M. Yu, E. Temeche, S. Indris and R. M. Laine, *Green Chem.*, 2021, 10.1039.D1GC02084F.
- 42 F. Yan, Y. D. Zheng, P. Chen, L. Sun and S. L. Gu, *Optical Materials*, 2003, **23**, 113–116.
- 43 P. Hu, S. Dong, X. Zhang, K. Gui, G. Chen and Z. Hu, *Sci Rep*, 2017, **7**, 3011.
- 44 W.-S. Seo, K. Koumoto and S. Aria, *Journal of the American Ceramic Society*, 2004, **83**, 2584–2592.
- 45 R. J. Iwanowski, K. Fronc, W. Paszkowicz and M. Heinonen, *Journal of Alloys and Compounds*, 1999, **286**, 143–147.
- 46 J. L. Blumenthal, M. J. Santy and E. A. Burns, *AIAA Journal*, 1966, **4**, 1053–1057.
- 47 C. Y. Chen, C. I. Lin and S. H. Chen, *British Ceramic Transactions*, 2000, **99**, 57–62.
- 48 A. W. Weimer, K. J. Nilsen, G. A. Cochran and R. P. Roach, *AIChE Journal*, 1993, **39**, 493–503.
- 49 N. Klinger, E. L. Strauss and K. L. Komarek, *Journal of the American Ceramic Society*, 1966, **49**, 369–375.

- 50 L.-F. Zhao, Z. Hu, W.-H. Lai, Y. Tao, J. Peng, Z.-C. Miao, Y.-X. Wang, S.-L. Chou, H.-K. Liu and S.-X. Dou, *Advanced Energy Materials*, 2021, **11**, 2002704.
- 51 C. Wang, Y. Li, K. (Ken) Ostrikov, Y. Yang and W. Zhang, *Journal of Alloys and Compounds*, 2015, **646**, 966–972.
- 52 B. J. Jeon and J. K. Lee, *Journal of Alloys and Compounds*, 2014, **590**, 254–259.
- 53 W. Wang, Y. Wang, L. Gu, R. Lu, H. Qian, X. Peng and J. Sha, *Journal of Power Sources*, 2015, **293**, 492–497.
- 54 X. D. Huang, F. Zhang, X. F. Gan, Q. A. Huang, J. Z. Yang, P. T. Lai and W. M. Tang, *RSC Advances*, 2018, **8**, 5189–5196.
- 55 D. Sri Maha Vishnu, J. Sure, H.-K. Kim, R. V. Kumar and C. Schwandt, *Energy Storage Materials*, 2020, **26**, 234–241.
- 56 Y. Hu, X. Liu, X. Zhang, N. Wan, D. Pan, X. Li, Y. Bai and W. Zhang, *Electrochimica Acta*, 2016, **190**, 33–39.
- 57 J. Liang, W. Wang, W. Yang, Z. Zhang, X. Zhang, Y. Jung and X. Dong, *Materials Chemistry and Physics*, 2020, **243**, 122618.
- 58 H. Zhang and H. Xu, *Solid State Ionics*, 2014, **263**, 23–26.
- 59 H. Zhang, X. Qin, J. Wu, Y. He, H. Du, B. Li and F. Kang, *J. Mater. Chem. A*, , DOI:10.1039/C4TA06044J.
- 60 L. Shi, C. Pang, S. Chen, W. Mingzhan, K. Wang, Z. Tan, J. Ren, Y. Huang, H. Peng and Z. Liu, *Nano letters*, , DOI:10.1021/acs.nanolett.7b00906.
- 61 L. Zhao, D. Jing, Y. Shi, Q. Zhuang, Y. Cui, Z. Ju and Y. Cui, *Ionics*, 2020, **26**, 4813–4824.
- 62 H. Li, H. Yu, X. Zhang, G. Guo, J. Hu, A. Dong and D. Yang, *Chem. Mater.*, 2016, **28**, 1179–1186.
- 63 Z. Zhao, H. Xie, J. Qu, H. Zhao, Q. Ma, P. Xing, Q. Song, D. Wang and H. Yin, *Batteries & Supercaps*, 2019, **2**, 1007–1015.
- 64 C. Sun, Y.-J. Wang, H. Gu, H. Fan, G. Yang, A. Ignaszak, X. Tang, D. Liu and J. Zhang, *Nano Energy*, 2020, **77**, 105092.
- 65 V. Agubra and J. Fergus, *Materials (Basel)*, 2013, **6**, 1310–1325.
- 66 X. Zhao and V.-P. Lehto, *Nanotechnology*, 2020, **32**, 042002.
- 67 C. Shao, F. Zhang, H. Sun, B. Li, Y. Li and Y. Yang, *Materials Letters*, 2017, **205**, 245–248.
- 68 J. Prasara-A and S. H. Gheewala, *Journal of Cleaner Production*, 2017, **167**, 1020–1028.

- 69 L. A. Middlemiss, A. J. R. Rennie, R. Sayers and A. R. West, *Energy Reports*, 2020, **6**, 232–241.
- 70 W. Choi, H.-C. Shin, J. M. Kim, J.-Y. Choi and W.-S. Yoon, *J. Electrochem. Sci. Technol.*, 2020, **11**, 1–13.
- 71 Q. Liu, Q. Shi, H. Wang, Q. Zhang and Y. Li, *RSC Adv.*, 2015, **5**, 47074–47079.
- 72 H. Zheng, Q. Qu, L. Zhang, G. Liu and V. S. Battaglia, *RSC Advances*, 2012, **2**, 4904–4912.
- 73 K. Wang, Y. Jin, S. Sun, Y. Huang, J. Peng, J. Luo, Q. Zhang, Y. Qiu, C. Fang and J. Han, *ACS Omega*, 2017, **2**, 1687–1695.
- 74 J. H. Park, H. Yoon, Y. Cho and C.-Y. Yoo, *Materials*, 2021, **14**, 4683.
- 75 T. Sun, X. Yao, Y. Luo, M. Fang, M. Shui, J. Shu and Y. Ren, *Ionics*, 2019, **25**, 4805–4815.
- 76 T. K. Bijoy, J. Karthikeyan and P. Murugan, *J. Phys. Chem. C*, 2017, **121**, 15106–15113.
- 77 J. R. Guth and W. T. Petuskey, *J. Phys. Chem.*, 1987, **91**, 5361–5364.
- 78 K. J. D. MacKenzie and M. E. Smith, Eds., in *Pergamon Materials Series*, Pergamon, 2002, vol. 6, pp. 201–268.
- 79 B. Walkley and J. L. Provis, *Materials Today Advances*, 2019, **1**, 100007.
- 80 H. Lechert, *Berichte der Bunsengesellschaft für physikalische Chemie*, 1988, **92**, 1059–1059.
- 81 J. Sanz, in *Defects and Disorder in Crystalline and Amorphous Solids*, ed. C. R. A. Catlow, Springer Netherlands, Dordrecht, 1994, pp. 157–188.
- 82 C. Dybowski, E. J. Gaffney, A. Sayir and M. J. Rabinowitz, *Colloids and Surfaces A: Physicochemical and Engineering Aspects*, 1996, **118**, 171–181.
- 83 K. Kitada, O. Pecher, P. C. M. M. Magusin, M. F. Groh, R. S. Weatherup and C. P. Grey, *J. Am. Chem. Soc.*, 2019, **141**, 7014–7027.
- 84 M. Letellier, F. Chevallier and F. Béguin, *Journal of Physics and Chemistry of Solids*, 2006, **67**, 1228–1232.
- 85 B. Key, R. Bhattacharyya, M. Morcrette, V. Seznéc, J.-M. Tarascon and C. P. Grey, *J. Am. Chem. Soc.*, 2009, **131**, 9239–9249.
- 86 R. Dedryvère, S. Leroy, H. Martinez, F. Blanchard, D. Lemordant and D. Gonbeau, *Journal of Physical Chemistry B*, DOI:10.1021/jp061624f.
- 87 S. Leroy, F. Blanchard, R. Dedryvère, H. Martinez, B. Carré, D. Lemordant and D. Gonbeau, *Surface and Interface Analysis*, DOI:10.1002/sia.2072.
- 88 C. Powell, 1989.
- 89 M. Yu, E. Temeche, S. Indris and R. M. Laine, *Green Chem.*, 2021, **23**, 7751–7762.

- 90 M. Jiao, Y. Wang, C. Ye, C. Wang, W. Zhang and C. Liang, *Journal of Alloys and Compounds*, 2020, **842**, 155774.
- 91 J. Moon, *International Journal of Energy Research*, 2021, **45**, 7315–7325.
- 92 C. C. Nguyen, H. Choi and S.-W. Song, *J. Electrochem. Soc.*, 2013, **160**, A906.
- 93 Y. Matsuo, J. Taninaka, K. Hashiguchi, T. Sasaki, Q. Cheng, Y. Okamoto and N. Tamura, *Journal of Power Sources*, 2018, **396**, 134–140.
- 94 T. Abe, in *Encyclopedia of Electrochemical Power Sources*, ed. J. Garche, Elsevier, Amsterdam, 2009, pp. 192–197.
- 95 J. R. Dahn, T. Zheng, Y. Liu and J. S. Xue, *Science*, , DOI:10.1126/science.270.5236.590.
- 96 P. Kurzweil, in *Electrochemical Energy Storage for Renewable Sources and Grid Balancing*, eds. P. T. Moseley and J. Garche, Elsevier, Amsterdam, 2015, pp. 269–307.
- 97 X. Zhao, N. Kalidas and V.-P. Lehto, *Journal of Power Sources*, 2022, **529**, 231269.
- 98 X. Zhang, E. Temeche and R. M. Laine, *Green Chem.*, 2020, **22**, 7491–7505.
- 99 E. Temeche, M. Yu and R. M. Laine, *Green Chem.*, 2020, **22**, 4656–4668.
- 100 N. Ding, J. Xu, Y. X. Yao, G. Wegner, X. Fang, C. H. Chen and I. Lieberwirth, *Solid State Ionics*, 2009, **180**, 222–225.
- 101 T. Schied, A. Nickol, C. Heubner, M. Schneider, A. Michaelis, M. Bobeth and G. Cuniberti, *ChemPhysChem*, 2021, **22**, 885–893.
- 102 Y. Zhu and C. Wang, *J. Phys. Chem. C*, 2010, **114**, 2830–2841.
- 103 G. Kresse and D. Joubert, *Physical Review B*, 1999, **59**, 1758–1775.
- 104 P. E. Blochl, *Physical Review B*, 1994, **50**, 17953–17979.
- 105 J. P. Perdew, A. Ruzsinszky, G. I. Csonka, O. A. Vydrov, G. E. Scuseria, L. A. Constantin, X. L. Zhou and K. Burke, *Physical Review Letters*, , DOI:10.1103/PhysRevLett.100.136406.
- 106 T. A. Manz and N. G. Limas, *Rsc Advances*, 2016, **6**, 47771–47801.